Facile Synthesis of Organic–Inorganic Hybrid Heterojunctions of Glycolated Conjugated Polymer-TiO<inf>2−X</inf> for Efficient

Downloaded from: https://research.chalmers.se, 2025-03-21 15:12 UTC

Citation for the original published paper (version of record):
Zhang, B., Wolkeba, Z., Wang, J. et al (2024). Facile Synthesis of Organic–Inorganic Hybrid Heterojunctions of Glycolated Conjugated
Polymer-TiO<inf>2−X</inf> for Efficient Photocatalytic Hydrogen Evolution. Small, 20(43).
http://dx.doi.org/10.1002/smll.202402649

N.B. When citing this work, cite the original published paper.

research.chalmers.se offers the possibility of retrieving research publications produced at Chalmers University of Technology. It covers all kind of research output: articles, dissertations, conference papers, reports etc. since 2004. research.chalmers.se is administrated and maintained by Chalmers Library

(article starts on next page)

Check for updates

RESEARCH ARTICLE

NANO · MICRO small
www.small-journal.com

Facile Synthesis of Organic–Inorganic Hybrid Heterojunctions of Glycolated Conjugated Polymer-TiO_{2-X} for Efficient Photocatalytic Hydrogen Evolution

Bingke Zhang, Zewdneh Genene, Jinzhong Wang, Dongbo Wang,* Chenchen Zhao, Jingwen Pan, Donghao Liu, Wenhao Sun, Jiefang Zhu,* and Ergang Wang**

The utilization of the organic–inorganic hybrid photocatalysts for water splitting has gained significant attention due to their ability to combine the advantages of both materials and generate synergistic effects. However, they are still far from practical application due to the limited understanding of the interactions between these two components and the complexity of their preparation process. Herein, a facial approach by combining a glycolated conjugated polymer with a TiO_{2-X} mesoporous sphere to prepare high-efficiency hybrid photocatalysts is presented. The functionalization of conjugated polymers with hydrophilic oligo (ethylene glycol) side chains can not only facilitate the dispersion of conjugated polymers in water but also promote the interaction with TiO_{2-X} forming stable heterojunction nanoparticles. An apparent quantum yield of 53.3% at 365 nm and a hydrogen evolution rate of 35.7 mmol h^{-1} g^{-1} is achieved by the photocatalyst in the presence of Pt co-catalyst. Advanced photophysical studies based on femtosecond transient absorption spectroscopy and in situ, XPS analyses reveal the charge transfer mechanism at type II heterojunction interfaces. This work shows the promising prospect of glycolated polymers in the construction of hybrid heterojunctions for photocatalytic hydrogen production and offers a deep understanding of high photocatalytic performance by such heterojunction photocatalysts.

1. Introduction

With the growing urgency to combat climate change and mitigate greenhouse gas emissions, there is an escalating need for green and renewable energy sources.[1–3] Hydrogen is an attractive primary energy source for a carbon-neutral society due to its excellent combustion properties, cleanliness, renewable nature, and ease of collection.[4,5] Inspired by natural photosynthesis, researchers are currently developing various photocatalysts. Photocatalytic hydrogen production from water splitting is regarded as one of the most promising energy production strategies available today.[6,7] Developing efficient and stable photocatalysts remains challenging due to the need to suppress electron–hole recombination, facilitate electron transfer, and meticulously manage light capture, energy levels, the photocatalytic interface, and the reaction mechanism.[8,9] In general, efficient photocatalytic hydrogen production materials must meet the following criteria: i) efficient absorption of a broad range of solar spectrum, ii) long charge-carrier lifetimes, and iii) minimal back-reaction rates.[10–12] Thus, photocatalysts based on heterojunctions have garnered widespread attention due to their potential to enhance the separation of photoexcited electron–hole pairs and facilitate cooperative light absorption, leading to a significant improvement in photocatalytic activity.[13,14]

In hybrid heterojunctions, well-defined structures can be formed between functionalized organic components and

B. Zhang, J. Wang, D. Wang, C. Zhao, J. Pan, D. Liu
Department of Optoelectronic Information Science, School of Materials Science and Engineering
Harbin Institute of Technology
Harbin 150001, China
E-mail: jinzhong_wang@hit.edu.cn; wangdongbo@hit.edu.cn

The ORCID identification number(s) for the author(s) of this article can be found under https://doi.org/10.1002/smll.202402649

© 2024 The Author(s). Small published by Wiley-VCH GmbH. This is an open access article under the terms of the Creative Commons Attribution-NonCommercial License, which permits use, distribution and reproduction in any medium, provided the original work is properly cited and is not used for commercial purposes.

DOI: 10.1002/smll.202402649

B. Zhang, J. Pan, W. Sun, J. Zhu
Department of Chemistry-Ångström Laboratory
Uppsala University
Uppsala SE-751 21, Sweden
E-mail: jiefang.zhu@kemi.uu.se

Z. Genene, E. Wang
Department of Chemistry and Chemical Engineering
Chalmers University of Technology
Göteborg SE-412 96, Sweden
E-mail: ergang@chalmers.se

J. Zhu
The Key Laboratory for Ultrafine Materials of The Ministry of Education
East China University of Science and Technology
Shanghai 200237, China

inorganic semiconductors by physical adsorption, stacking forces, or covalent bonding. The charge transfer mechanism of hybrid heterojunctions can consist of three different pathways: i) sensitization; ii) type II heterojunction; and iii) S-scheme heterojunction.[15] All three pathways would be favorable for wide light absorption, highly efficient charge transfer, and low recombination of photogenerated electrons and holes, thereby improving photocatalytic performance.[16] Organic conjugated polymers have been used in photocatalysis due to their structural tunability, high absorption coefficients, and broad absorption spectra.[17–20] Recently conjugated polymers have received much attention due to their tunable bandgap from 1 to 3 eV,[21] and excellent visible-light-driven hydrogen evolution function.[22,23] However, due to the charge carriers in linear conjugated polymers often suffer from short lifetime and low mobility, and most reported conjugated polymer-based materials possess hydrophobic alkyl side chains that result in poor water solubility, it is still very challenging for conjugated polymers to achieve efficient photocatalytic hydrogen evolution.[24–26] To enhance photocatalytic performance, rational design of both the polymer backbone and side substituents is necessary for synthesizing conjugated polymers.[27,28] On one hand, utilizing the high π-electron density of thiophene and its derivatives in photocatalysis-related polymers helps reduce exciton binding energy and suppress charge carrier recombination. These polymers have strong absorption in the visible region due to their unique chromophores in π-conjugated chains.[29] Additionally, the high polarizability of the sulfur atoms in the thiophene ring promotes the stability of the conjugated chain and optimizes the charge transport properties.[30] On the other hand, employing hydrophilic side chain modifications in conjugated polymers as organic photocatalysts for hydrogen evolution, especially functionalizing conjugated polymers with oligo(ethylene glycol) (OEG) side chains, significantly lowers the energy levels on the polymer surface by adsorbing H^+ from water. This notably enhances the photocatalytic performance compared to alkyl-functionalized conjugated polymers.[31–33] Such hydrophilic conjugated polymers with both semiconducting conjugated scaffolds and hydrophilic side chains have good dispersibility/solubility in polar solvents and water.[34,35] However, high-efficiency hydrogen evolution of hybrid heterojunctions based on hydrophilic conjugated polymers has been rarely reported. Such conjugated polymers functionalized with hydrophilic OEG side chains are expected to combine with inorganic semiconductors to form novel organic–inorganic hybrid photocatalysts.

In hybrid heterojunctions, TiO_2 is widely used as an inorganic semiconductor due to its remarkable chemical stability, low cost, nontoxicity, and high redox capability.[36–38] In recent years, the incorporation of oxygen vacancy in TiO_{2-X} through structural engineering has proven to be a highly effective approach in enhancing photocatalytic performance.[39,40] The controlled introduction of defects can capture electrons and prevent the recombination of electron–hole pairs, thus prolonging their lifetime.[41] However, despite the existence of oxygen vacancies that can create defect energy levels and extend light absorption to the visible spectrum, hydrogen production efficiency under visible light irradiation is still quite low, due to the limited number of oxygen vacancies formed by most methods.[42,43] Hence, it can be interesting to employ conjugated polymers with suitable band alignment and excellent visible light absorption to construct heterostructures with TiO_{2-X}, fulfilling efficient photocatalytic applications. Hybrid materials combining polymers and TiO_2 have been developed for H_2 production. However, they exhibit relatively low apparent quantum yield (AQY) and hydrogen evolution rates (HER) (Table S1, Supporting Information). Furthermore, the mechanism of interfacial charge carrier transfer between the two components in hybrid heterojunctions urgently needs to be studied in detail.

Therefore, we develop heterojunction photocatalysts by combining conjugated polymer poly[2,5-bis(thiophenyl)-1,4-bis(2-(2-(2-methoxyethoxy)ethoxy)-ethoxy)benzene] (PB2T-TEG) with TiO_{2-X} mesoporous sphere (MS) to improve photocatalytic performance.[44] PB2T-TEG consisting of benzene attached with OEG side chains and bithiophene units was selected due to its low cost and the fact that the OEG side chains can not only facilitate ion uptake and transport but facilitate the interaction with TiO_{2-X}.[45,46] Furthermore, this conjugated polymer with coplanar molecular structure and high electron acceptability is combined with TiO_{2-X} to form an organic–inorganic heterojunction PB2T-TEG-TiO_{2-X}. Under simulated solar light, the heterojunction achieves the highest HER of 35.7 mmol h^{-1} g^{-1} and maintains a stable hydrogen evolution over a 16-h water splitting process, with AQY as high as 53.3% at 365 nm and 11.1% at 500 nm using only 0.62 wt.% Pt co-catalyst, one of the highest AQY for TiO_{2-X}-based materials. Femtosecond transient absorption (fs-TA) spectroscopy and in situ X-ray photoelectron spectroscopy (XPS) were further carried out to verify the proposed mechanism at the PB2T-TEG-TiO_{2-X} heterojunction.

2. Results and Discussion

2.1. Morphology and Structure of PB2T-TEG-TiO_{2-X}

The structure and synthesis of PB2T-TEG-TiO_{2-X} are shown in **Figure 1a**. The polymer PB2T-TEG was synthesized by Stille polymerization from dibromobenzene attached with OEG side chains and 5,5′-bis(trimethylstannyl)-2,2′-bithiophene. The procedure of polymer synthesis is described in the Experimental Section. The polymer is soluble in chloroform and dispersible in ethanol. The ^1H NMR spectra showed characteristic signals of the OEG side chains at 3.3–7.6 ppm, indicating that hydrophilic non-conjugated groups were present in the polymer (Figure S1, Supporting Information). The number-average molecular weight (Mn) and dispersity (Đ) of the polymer were 41 kDa and 1.5, respectively, determined by size exclusion chromatography in dimethylformamide. The oxygen-doped semiconductor TiO_{2-X} mesoporous nanospheres that were obtained by high-temperature hydrogen reduction were dispersed in ethanol. Subsequently, the ethanol dispersion of TiO_{2-X} was mixed with the PB2T-TEG ethanol solution under ultrasonication and the mixture was heated while stirring to form composite materials. In order to optimize the performance of the heterojunction, the contents of PB2T-TEG were varied to be 1, 3, 5, and 7 wt.% relative to TiO_{2-X}. The prepared samples were denoted as TiO_{2-X}-PY (Y = 1,3,5,7), e.g. the PB2T-TEG content of 3 wt.% was denoted as TiO_{2-X}-P3. In the ethanol dispersion, the TiO_{2-X} and PB2T-TEG samples had opposite charges, allowing the construction of TiO_{2-X}-PY through the electrostatic interactions between

© 2024 The Author(s). Small published by Wiley-VCH GmbH

16136829, 2024, 43, Downloaded from https://onlinelibrary.wiley.com/doi/10.1002/smll.202402649 by Statens Beredning, Wiley Online Library on [14/11/2024]. See the Terms and Conditions (https://onlinelibrary.wiley.com/terms-and-conditions) on Wiley Online Library for rules of use; OA articles are governed by the applicable Creative Commons License

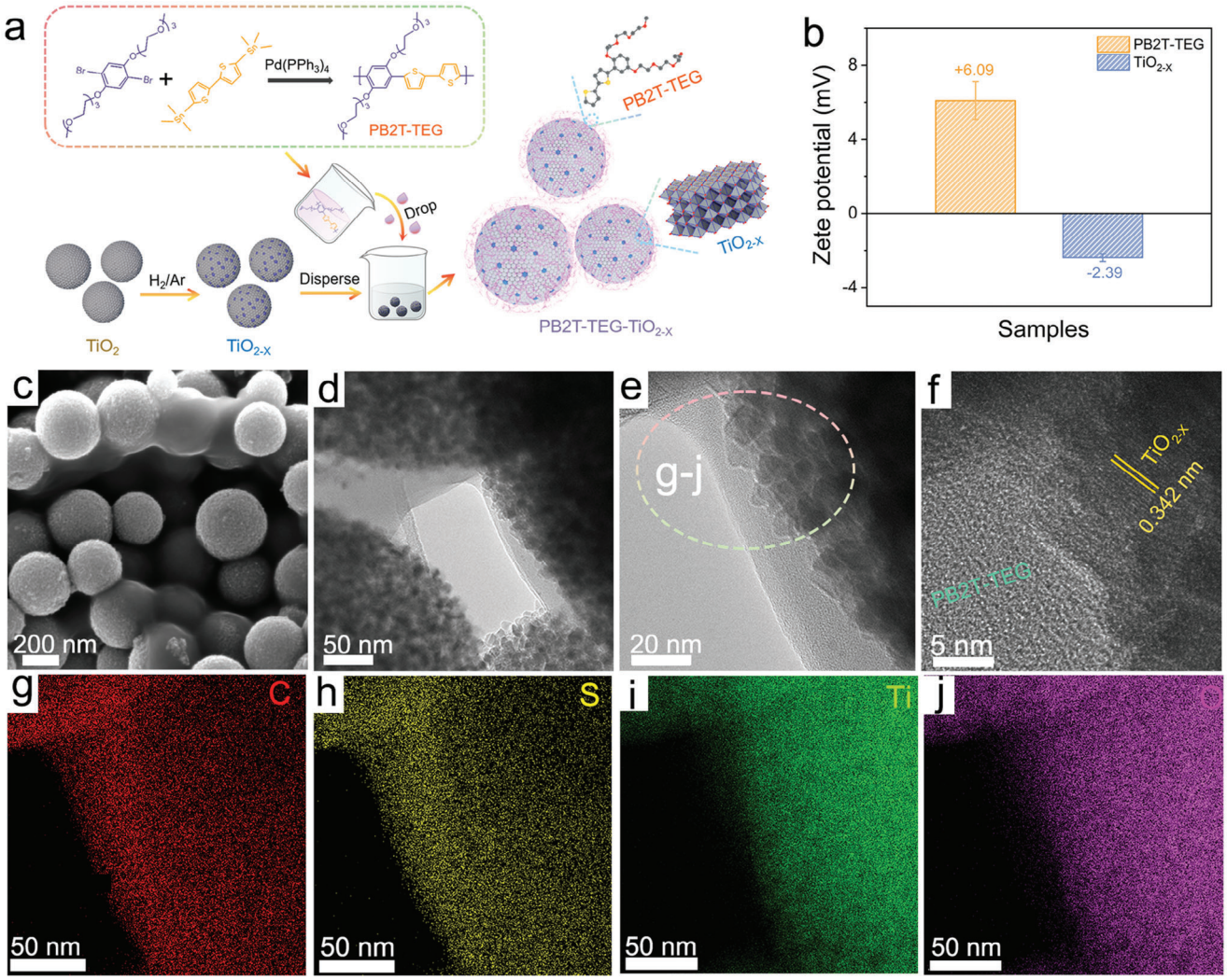

Figure 1. a) Schematic representation of the preparation of PB2T-TEG-TiO_{2-X}, b) Zeta potentials of PB2T-TEG and TiO_{2-X}, c) SEM image of TiO_{2-X}-P3, d, e) TEM image of TiO_{2-X}-P3, f) HRTEM image of TiO_{2-X}-P3, g–j) EDS mapping of TiO_{2-X}-P3.

TiO_{2-X} and PB2T-TEG (Figure 1b). The microscopic morphology of the heterojunction was observed by scanning electron microscopy (SEM), in which TiO_{2-X} is a mesoporous nanosphere with a rough surface (Figure S2, Supporting Information). As shown in Figure 1c, PB2T-TEG of graphene-like layered assemblies is randomly wrapping around the mesoporous TiO_{2-X} nanospheres, suggesting the existence of close interactions between PB2T-TEG and TiO_{2-X}. The disposition of PB2T-TEG over the TiO_{2-X} mesoporous sphere was unequivocally confirmed by transmission electron microscopy (TEM) (Figure 1d,e). The high-resolution transmission electron microscopy (HRTEM) images also clearly showed the existence of a distinct heterogeneous interface between PB2T-TEG and TiO_{2-X} (Figure 1f). The lattice strip spacing of TiO_{2-X} is 0.342 nm, corresponding to the lattice plane of anatase TiO_2 (101).[47] However, due to its lower crystallinity, the lattice stripes of amorphous PB2T-TEG are indistinguishable. Nevertheless, pure TiO_{2-X} exhibits notably clear and uncovered grain surfaces (Figure S3, Supporting Information). The energy-dispersive spectroscopy (EDS) was further employed for elemental mapping. The results confirmed that C, S, O, and Ti elements are evenly distributed within the TiO_{2-X}-P3 nanostructure, and the S distribution indicates the successful encapsulation of PB2T-TEG on TiO_{2-X} (Figure 1g–j).

Powder X-ray diffraction (PXRD) confirmed the crystal structure of PB2T-TEG-TiO_{2-X}, as shown in **Figure 2a**. The diffraction peaks at 25.4°, 38.2°, 48.1°, 54.1°, 55.0°, 63.5°, 69.1°, 70.4°, and 75.3° can be indexed to (101), (004), (112), (200), (105), (211), (204), (116), (220) and (215) crystal planes of anatase TiO_2 (JCPDS card No. 21–1272), respectively.[48] TiO_{2-X} MS has a similar crystal structure with pristine TiO_2 MS (Figure S4, Supporting Information), indicating that TiO_{2-X} has good structural stability during high-temperature hydrogen reduction. Compared with TiO_2 MS, the (101) diffraction peak intensity of TiO_{2-X} MS decreases, and the full width at half maximum (FWHM) broadens due to oxygen vacancies and Ti^{3+} doping.[49] The presence of a diffraction peak at 7.3° is attributed to the polymer PB2T-TEG. The peaks of TiO_{2-X} and PB2T-TEG are clearly observed in all prepared composite materials. The samples were observed

© 2024 The Author(s). Small published by Wiley-VCH GmbH

16136829, 2024, 43, Downloaded from https://onlinelibrary.wiley.com/doi/10.1002/smll.202402649 by Statens Beredning, Wiley Online Library on [14/11/2024]. See the Terms and Conditions (https://onlinelibrary.wiley.com/terms-and-conditions) on Wiley Online Library for rules of use; OA articles are governed by the applicable Creative Commons License

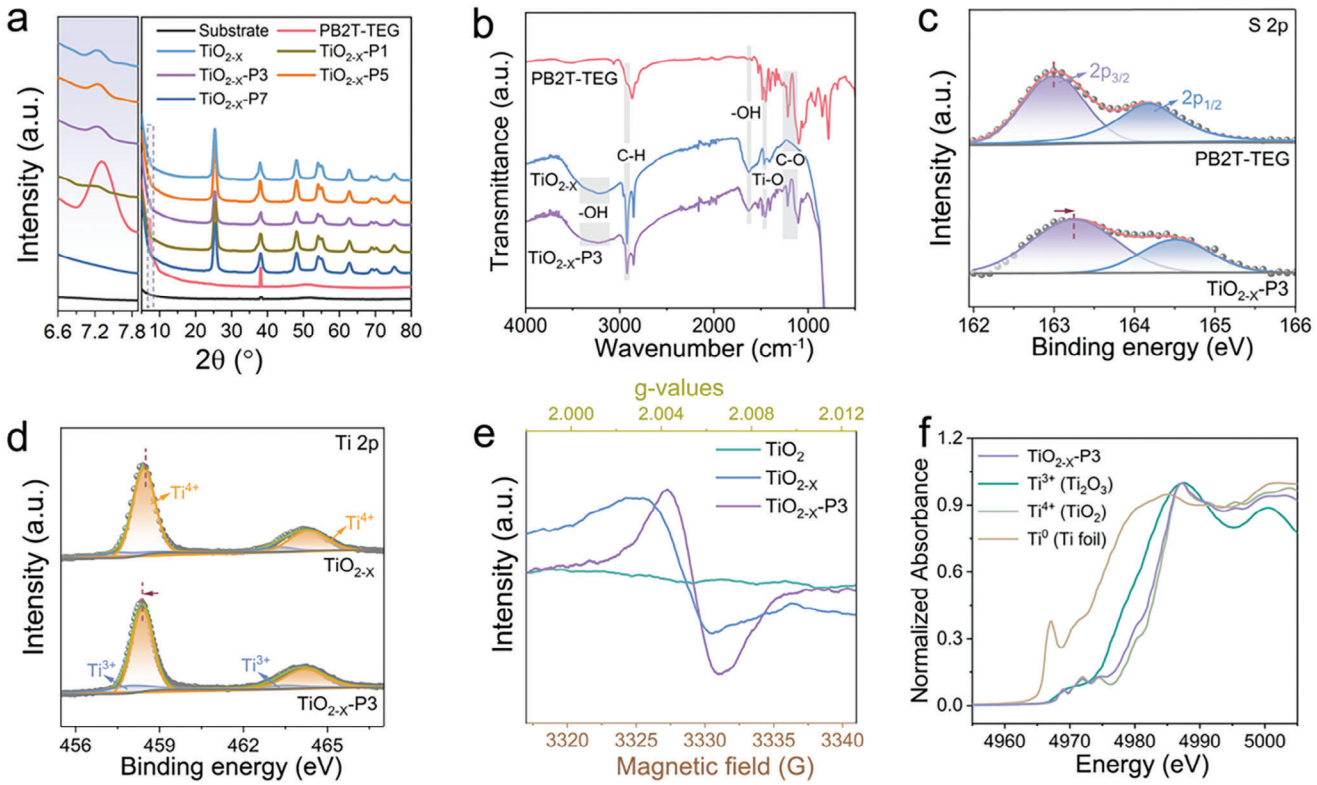

Figure 2. a) PXRD patterns, b) FTIR, c) High-resolution Ti 2p XPS spectrum of TiO_{2-X}-P3, d) High-resolution S 2p XPS spectrum of PB2T-TEG and TiO_{2-X}-P3, e) EPR spectra of PB2T-TEG, TiO_{2-X} and TiO_{2-X}-P3, f) Ti-K edge XANES of TiO_{2-X}-P3 compared to the model compounds Ti foil, Ti_2O_3 and TiO_2.

with Fourier transform infrared spectrometer (FTIR) spectra, as shown in Figure 2b. In the FTIR spectrum of TiO_{2-X}-P3, there were strong peaks at 1085 and 1157 cm^{-1}, attributed to C—O stretching vibrations resulting from PB2T-TEG molecules. The peaks at 1632 cm^{-1} and broad IR bands ≈3600–3000 cm^{-1} originate from the absorption of water or —OH groups.[50] The peaks at 2932 cm^{-1} are attributed to the C—O bond.[51] The absorption peak at 1380 cm^{-1} demonstrates the vibration of Ti—O.[52] FTIR spectra showed the characteristic bands of the TiO_{2-X}-P3 contain the PB2T-TEG and TiO_{2-X} cores, thus confirming the successful synthesis of hybrid heterojunctions. In Figure 2c, the incorporation of thiophene units resulted in the detection of S 2p peaks in the TiO_{2-X}-P3 heterostructure with a notable shift toward higher energy compared to the S 2p peak of PB2T-TEG alone by XPS at a detection depth of ≈10 nm, suggesting that the organic PB2T-TEG is grafted onto TiO_{2-X}.[53] As shown in Figure S5 (Supporting Information), the high-resolution O 1s spectrum of TiO_{2-X}-P3 can be fitted into three peaks of 529.5, 531.0, and 533.5 eV, which could be attributed to lattice oxygen, —OH and C—O bonds,[54,55] respectively. Furthermore, additional small peaks associated with defect-induced Ti^{3+} can be observed in the high-resolution spectrum of TiO_{2-X}-P3 for Ti 2p (Figure 2d). Similarly, electron paramagnetic resonance (EPR) tests were carried out to investigate the defects in the photocatalysts, and it can be seen that after high-temperature hydrogen reduction, characteristic peaks attributed to oxygen defects appear in the black TiO_{2-X} (e.g., surface Ti^{IV}—O centers, with g values >2.0023) compared to TiO_2 MS (Figure 2e).[56] While in TiO_{2-X}-P3 the EPR response is stronger due to the presence of unpaired electrons on the aromatic ring carbon atoms of PB2T-TEG.[57] The X-ray absorption near edge structure (XANES) spectrum for as-prepared TiO_{2-X}-P3 was compared with those for authentic Ti(0), Ti(III), and Ti(IV) models in Figure 2f. Although the detailed structure of the XANES spectrum of TiO_{2-X}-P3 is basically the same as that of the Ti(IV) model compound, the slight edge shift to lower energy for TiO_{2-X}-P3 is consistent with Ti(III), suggesting that the oxidation state of Ti in the as-prepared TiO_{2-X}-P3 is a mixture of Ti^{4+} and Ti^{3+}.[58]

2.2. Optical Properties and Charge Transfer

The optical absorption and electronic structure of photocatalysts are important factors affecting hydrogen production. The optical absorption of the samples was characterized by UV–vis diffuse reflectance spectroscopy. The spectra are illustrated in **Figure 3a** and Figure S6 (Supporting Information). Pure TiO_2 exhibits strong absorption in the ultraviolet region, with negligible absorption in the visible region. However, defective doping and the incorporation of PB2T-TEG led to a significant enhancement of absorption in the visible region for TiO_{2-X}-P3. This enhancement implies that the heterojunction may generate more charge carriers under visible light irradiation. The inset of Figure 3a

© 2024 The Author(s). Small published by Wiley-VCH GmbH

16136829, 2024, 43, Downloaded from https://onlinelibrary.wiley.com/doi/10.1002/smll.202402649 by Statens Beredning, Wiley Online Library on [14/11/2024]. See the Terms and Conditions (https://onlinelibrary.wiley.com/terms-and-conditions) on Wiley Online Library for rules of use; OA articles are governed by the applicable Creative Commons License

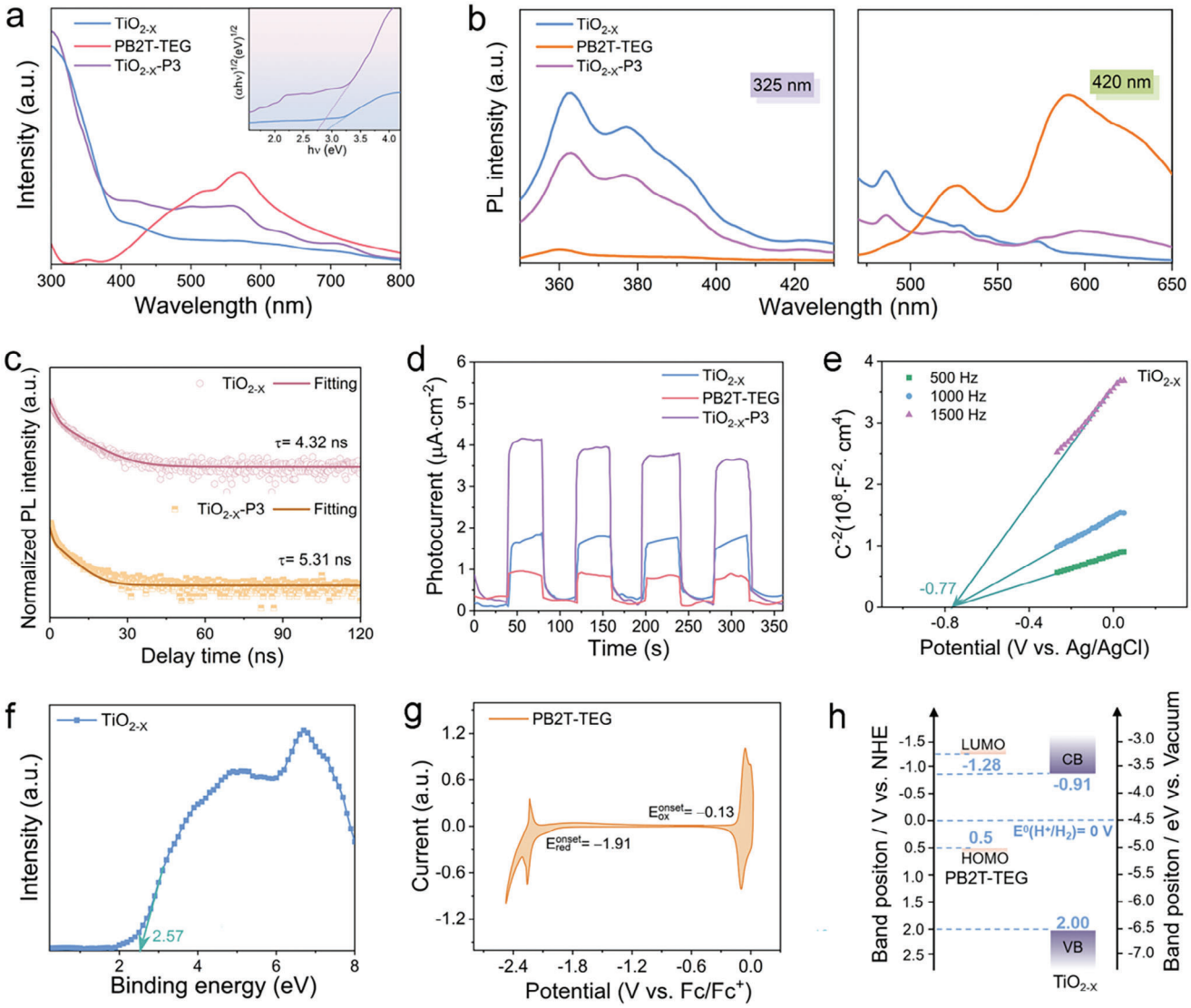

Figure 3. a) UV–vis absorption spectra of PB2T-TEG, TiO_{2-X}, and TiO_{2-X}-P3 (inset: Tauc diagrams of TiO_{2-X} and TiO_{2-X}-P3), b) Steady-state PL spectra (λ_{exc}=325 and 420 nm), c) Time-resolved photoluminescence of TiO_{2-X} and TiO_{2-X}-P3 recorded at 520 nm (excited by 375 nm excitation pulse), d) Transient photocurrent responses of PB2T-TEG, TiO_{2-X} and TiO_{2-X}-P3, e) MS of TiO_{2-X}, f) VB-XPS of TiO_{2-X}, g) Cyclic voltammetry of PB2T-TEG measured in acetonitrile containing 0.1 M $[(nBu)_4)N]PF_6$ as electrolyte, h) Proposed band structure of PB2T-TEG and TiO_{2-X}.

also shows Tauc diagrams with estimated band gaps of 2.91 and 2.75 eV for TiO_{2-X} and TiO_{2-X}-P3, respectively.[59]

To examine the impact of TiO_{2-X}-P3 heterojunction on the photo-induced electron separation and transfer, steady-state photoluminescence (PL), time-resolved photoluminescence (TRPL) spectroscopy measurements, and electrochemical tests were conducted. The PL emission peak of black TiO_{2-X} under excitation at 325 nm is attributed to band-to-band recombination, which weakens upon the formation of a heterojunction with PB2T-TEG (Figure 3b). Corresponding to the UV/Vis absorption, PB2T-TEG does not exhibit a PL emission peak due to its lack of optical absorption in the ultraviolet region. Under 420 nm excitation, the PL intensity of TiO_{2-X}-P3 decreases dramatically compared to pure PB2T-TEG, indicating that the construction of the heterojunction significantly improves charge/energy transfer.[60] To gain in-depth insights into the charge transfer dynamics, TRPL decay measurements were performed (Figure 3c; Table S2, Supporting Information). The TiO_{2-X}-P3 heterojunction shows an increased average emission lifetime (τ = 5.31 ns) compared to black TiO_{2-X} (τ = 4.32 ns), indicating that faster electron transfer and slower charge recombination in TiO_{2-X}-P3. The same conclusion can be obtained through electrochemical impedance spectroscopy (EIS) measurement as well. It reveals photoinduced electron–hole separation and charge transfer resistance within the TiO_{2-X}-P3 heterojunction, as shown in Figure S7 (Supporting Information). Typically, the charge transfer resistance is reflected through the Nyquist curve, where a smaller diameter of the semicircular arc indicates higher efficiency in electron–hole separation and transfer.[61] Apparently, the TiO_{2-X}-P3 heterostructure presents smaller arcs than that of TiO_{2-X} and

 © 2024 The Author(s). Small published by Wiley-VCH GmbH

16136829, 2024, 43, Downloaded from https://onlinelibrary.wiley.com/doi/10.1002/smll.202402649 by Statens Beredning, Wiley Online Library on [14/11/2024]. See the Terms and Conditions (https://onlinelibrary.wiley.com/terms-and-conditions) on Wiley Online Library for rules of use; OA articles are governed by the applicable Creative Commons License

PB2T-TEG, indicating that TiO_{2-X}-P3 has weaker electronic impedance and enhanced charge separation and transfer efficiency. The photocurrents of PB2T-TEG, TiO_{2-X}, and TiO_{2-X}-P3 were measured via several on–off cycles under intermittent UV light irradiation, correlating with the separation efficiency of the photogenerated charge carriers. As shown in Figure 3d, the photocurrent responses of all samples are stable and reproducible in the time scale of 360 s, and the transient photocurrent of TiO_{2-X}-P3 turns out to be ≈2.4 times and 4.3 times higher than those of TiO_{2-X} and PB2T-TEG, respectively. All these results illustrate that the formation of heterojunction promotes efficient electron–hole separation. As expected, the linear sweep voltammetry (LSV) of these samples also displayed that the TiO_{2-X}-P3 heterojunction yielded the highest photocurrent density (Figure S8, Supporting Information). The enhanced photoelectric properties of TiO_{2-X}-P3 can be attributed to increased charge carrier mobility in the heterojunction structure.

In addition, the relative positions of the energy bands of TiO_{2-X} and PB2T-TEG play an important role in determining electron transfer in photocatalysis. Thus, the band positions are also studied in detail. The electrochemical impedance measurements were conducted on the pristine TiO_{2-X} to evaluate their flat band potentials. As demonstrated in Figure 3e, the positive slopes of the extension lines at 500, 1000, and 1500 Hz frequencies exhibited the n-type semiconductor features of as-prepared TiO_{2-X}, and the flat-band potentials of the TiO_{2-X} is estimated to be −0.77 V (vs Ag/AgCl), suggesting Fermi levels locate at −0.57 V (vs NHE).[62] The valence band (VB) positions were inferred from valence band X-ray photoelectron spectroscopy (VB-XPS) for the inorganic semiconductor TiO_{2-X}. As shown in Figure 3f, the distance between VB and Fermi level of TiO_{2-X} is reckoned to be 2.57 eV. Naturally, the TiO_{2-X} samples have the VB position of 2.00 eV. Furthermore, based on the energy gaps (E_g) of TiO_{2-X} from UV–vis absorption and the VB from the VB-XPS spectrum, the conduction band (CB) for the sample was calculated using the formula: $E_{CB} = E_{VB} + E_g$,[63] which is −0.91 V for electrode potential (V vs NHE). Regarding the electronic structure of the hybrids, the relative energy levels of the highest occupied molecular orbital (HOMO) and the lowest unoccupied molecular orbital (LUMO) of the polymers were estimated by the electrochemical determination of their ionization potential (IP) and electron affinity (EA). For the PB2T-TEG, HOMO was calculated to be −5.00 eV, and LUMO was −3.22 eV versus Vacuum, according to its oxidation and reduction potentials (0.5 and −1.28 V vs NHE, respectively) from cyclic voltammetry (CV) measurements (Figure 3g). PB2T-TEG exhibited a bandgap of 1.78 eV, according to its HOMO and LUMO energies. Based on the above-mentioned results, the band structure diagrams of TiO_{2-X} and PB2T-TEG are illustrated in Figure 3h, which indicates a Type II energy level alignment and fulfills the thermodynamic requirements for driving H_2 evolution.

2.3. Photocatalytic Activity

The photocatalytic H_2 evolution was implemented under simulated sunlight AM 1.5G with Pt as a co-catalyst and triethanolamine as a sacrificial reagent. **Figure 4a** depicts the cumulative hydrogen production versus time for PB2T-TEG, $TiO_{2-X,}$ and TiO_{2-X}-P3 catalysts. The pristine polymer PB2T-TEG exhibits poor HER performance due to the rapid recombination of photo-induced electrons and holes. Meanwhile, in a series of hybrid TiO_{2-X}-PY (Y = 1, 3, 5, 7 wt.%), the photocatalytic activity shows a trend of initially increasing and then decreasing with the amount of PB2T-TEG. The initial increase can be explained by the strong absorption of the polymer PB2T-TEG and the subsequent decrease is mainly due to the excessive coverage of the active sites by the excess of PB2T-TEG. The HER of the TiO_{2-X}-P3 could reach 35.7 mmol g^{-1} h^{-1} at the dosage of 3 wt.% PB2T-TEG, which is 2.8 and ≈221 times higher than those of TiO_{2-X} (12.9 mmol g^{-1} h^{-1}) and PB2T-TEG (0.161 mmol g^{-1} h^{-1}), respectively. The results show that there is a synergistic effect between organic and inorganic semiconductors in heterostructures.

It is well known that one of the main limitations of polymer photocatalytic applications is their limited photochemical stability. In fact, linear polymers tend to degrade under prolonged light exposure. Here, an extended 16-h hydrogen production was conducted to assess the stability of the photocatalyst. Throughout the entire duration, the hydrogen evolution remained consistently stable, demonstrating total H_2 production of 495.85 mmol g^{-1} in 16 h (Figure 4b). Even without the co-catalyst Pt, the HER of TiO_{2-X}-P3 can still reach 8.6 mmol g^{-1} h^{-1} (Figure S9, Supporting Information). To further highlight the contribution of PB2T-TEG to hydrogen production in the heterojunction, hydrogen production was investigated under UV light only, outside of the PB2T-TEG absorption range, and the HER of TiO_{2-X}-P3 is only twice as high as that of TiO_{2-X}. Furthermore, the photostability of TiO_{2-X}-P3 was characterized by XPS analysis of the recovered TiO_{2-X}-P3 after the photocatalytic reaction for 16 h, and no significant change is observed in comparison with the fresh TiO_{2-X}-P3 catalysts (Figure 2c; Figure S10, Supporting Information). Especially, Ti^{3+} has strong stability before and after photocatalytic reaction (Figure 2d; Figure S10c, Supporting Information). Both PXRD and TEM demonstrated the structural, compositional, and morphological stability of the TiO_{2-X}-P3 heterojunction during the photocatalytic process (Figures S11 and S12, Supporting Information).

Meanwhile, the high-resolution Pt 4f XPS spectrum of TiO_{2-X}-P3 after the photocatalytic reaction revealed that the in situ anchored Pt remained on TiO_{2-X}-P3 (Figure S12, Supporting Information), confirming the high stability of metallic Pt on the TiO_{2-X}-P3.[64] AQY was obtained under the illumination of a 300 W xenon lamp with different wavelength band-pass filters (λ = 365, 410, 460, 500, 600 nm).[65] TiO_{2-X}-P3 exhibits AQYs of 53.3% and 11.1% at 365 and 500 nm, respectively, with a co-catalyst Pt content of 0.62 wt.% (Figure 4c; Table S3, Supporting Information). The trend in AQY as a function of wavelength matches with the UV–vis absorption spectrum of TiO_{2-X}-P3, indicating that photocatalytic hydrogen evolution indeed occurred upon light harvesting. To the best of our knowledge, TiO_{2-X}-P3 presents one of the highest activities reported for photocatalytic H_2 evolution and could provide a pathway for efficient solar-to-chemical energy conversion by significantly improving the solar-to-hydrogen conversion efficiency of the current hybrid heterojunction (Figure 4d; Table S1, Supporting Information).[66]

© 2024 The Author(s). Small published by Wiley-VCH GmbH

16136829, 2024, 43, Downloaded from https://onlinelibrary.wiley.com/doi/10.1002/smll.202402649 by Statens Beredning, Wiley Online Library on [14/11/2024]. See the Terms and Conditions (https://onlinelibrary.wiley.com/terms-and-conditions) on Wiley Online Library for rules of use; OA articles are governed by the applicable Creative Commons License

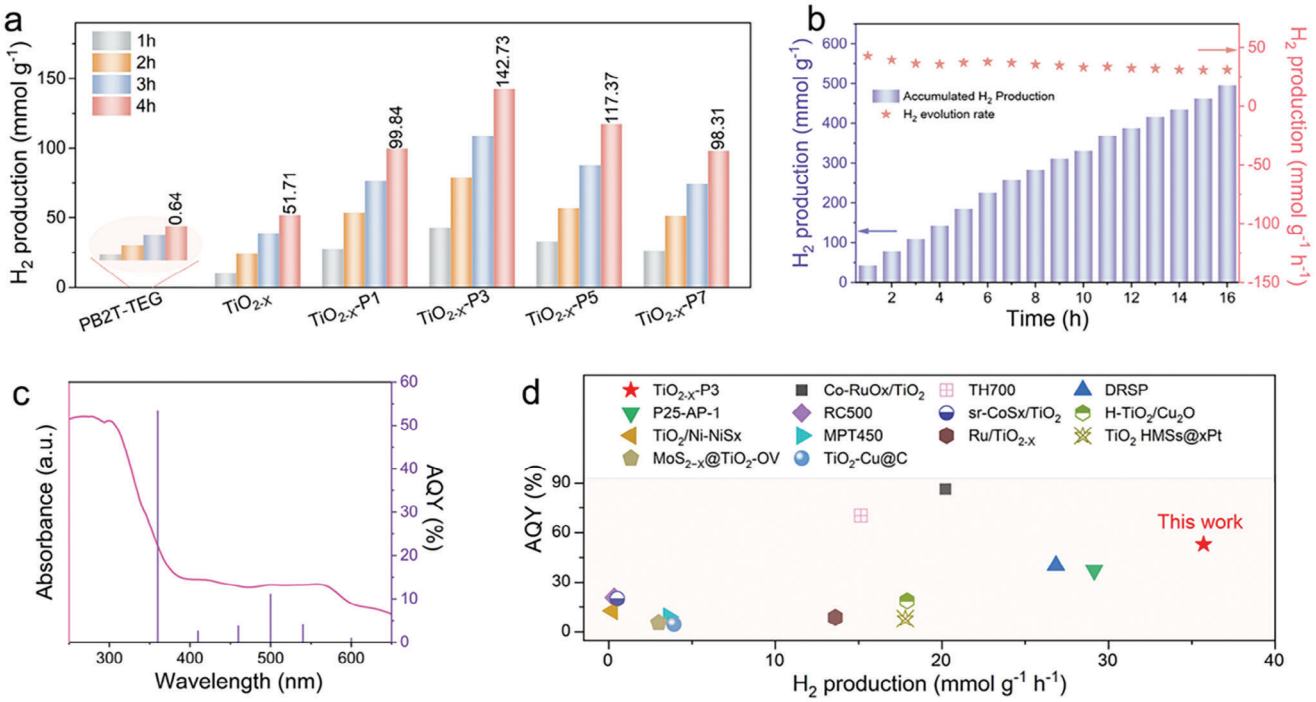

Figure 4. a) The cumulative hydrogen production versus time by PB2T-TEG, TiO_{2-X}, and TiO_{2-X}-PY (Y = 1, 3, 5, 7 wt.%) photocatalysts, b) H_2 evolution versus time by TiO_{2-X}-P3 over a period of 16 h, c) Correlation between the AQY and the UV–vis absorption spectrum of TiO_{2-X}-P3, d) Comparison of photocatalytic H_2 evolution rate and AQY of TiO_{2-X}-P3 with various TiO_2-base photocatalysts reported previously, All photocatalysts are compared with the AQY at 365 nm. See Table S1 (Supporting Information) for more detailed information).

2.4. Photocatalytic Mechanism Analysis

To clarify the charge transfer process and understand the improved photocatalytic activity of the hybrids, fs-TA spectroscopy (**Figure** 5a–h) using the pump-probe technique under 315 nm laser excitation and high-resolution in situ XPS measurements for Ti 2p states of TiO_{2-X}-P3 were conducted (**Figure** 6a). As shown in Figure 5a,d, the TA spectrum of PB2T-TEG shows an obvious negative peak at ≈576 nm after excitation by a pump pulse with a wavelength of 315 nm, which belongs to ground state bleaching (GSB).[67] Figure 5b,e displays the fs-TA spectroscopy for TiO_{2-X}, two GSB peaks can be clearly observed in the wide wavelength range of ≈340 nm and 512–640 nm on the microsecond-second time scale, which are in good agreement with the absorption edge of TiO_{2-X}. In addition to the GSB peaks, a positive peak with a wavelength of ≈423 nm is observed in the fs-TA spectrum of TiO_{2-X}, which is a spectral feature attributed to the excited state absorption (ESA) of the trapped holes on the defect state. As shown in Figure 5c,f, GSB signals dominated by PB2T-TEG appear at the TiO_{2-X}-P3 heterojunction at 584 nm. It is obvious that the GSB peak of PB2T-TEG in the TiO_{2-X}-P3 heterostructure is redshifted, which is probably caused by the introduction of strain at the interface of the heterostructure or the change of the built-in electrical field of the heterostructure.[68] Thus, the decay times were further studied in the PB2T-TEG, TiO_{2-X}, and TiO_{2-X}-P3 composite. Figure 5g shows the kinetic profiles of TiO_{2-X} and TiO_{2-X}-P3 absorption at 340 nm. The decay traces were fitted to a three-exponential model, demonstrating that three pathways dominate the relaxation of photo-generated electrons (as shown in Table S4, Supporting Information). For the TiO_{2-X}-P3 composite, in addition to the very short diffusion lifetime of a few picoseconds (τ_1 = 4.8 ps) for the electrons on the lattice, two slower relaxation processes can be explained by the trapped states (τ_2 = 172 ps) and recombination of electrons in CB with holes in VB (τ_3 = 12 400 ps), respectively. Notably, TiO_{2-X}-P3 shows a longer electron diffusion lifetime than TiO_{2-X}, implying that the photogenerated charges can migrate further before decaying back to the ground state, leading to more efficient electron–hole separation.[69] Further, the GSB decay signal at the peak corresponding to the PB2T-TEG bleaching peak was fitted using a four-exponential function since the interfacial electron-transfer process (Figure 5h; Table S4, Supporting Information). The newly fitted lifetime (τ_4) attributable to interfacial electron transfer is 19.2 ps in TiO_{2-X}-P3, in addition to the lifetimes attributed to electron diffusion on the lattices, carrier transfer to the trap states, conduction band electron, and valence band hole recombination.[70] The electron transfer direction at the heterojunction interface can be further tested by in situ XPS.

During the XPS measurement process, three different lighting conditions were employed: dark, UV light, and visible light. Notably, as shown in Figure 6b, the binding energy of Ti 2p for TiO_{2-X}-P3 showed a noticeable negative shift upon visible light irradiation, in contrast to that under dark conditions, suggesting that more electrons are accumulated on TiO_{2-X}. Similarly, the Ti 2p binding energy of TiO_{2-X}-P3 exhibits a more pronounced negative shift under UV irradiation. ESR was performed to further explore the photocatalytic mechanism model by detecting the production of the reactive species in this system under

© 2024 The Author(s). Small published by Wiley-VCH GmbH

16136829, 2024, 43, Downloaded from https://onlinelibrary.wiley.com/doi/10.1002/smll.202402649 by Statens Beredning, Wiley Online Library on [14/11/2024]. See the Terms and Conditions (https://onlinelibrary.wiley.com/terms-and-conditions) on Wiley Online Library for rules of use; OA articles are governed by the applicable Creative Commons License

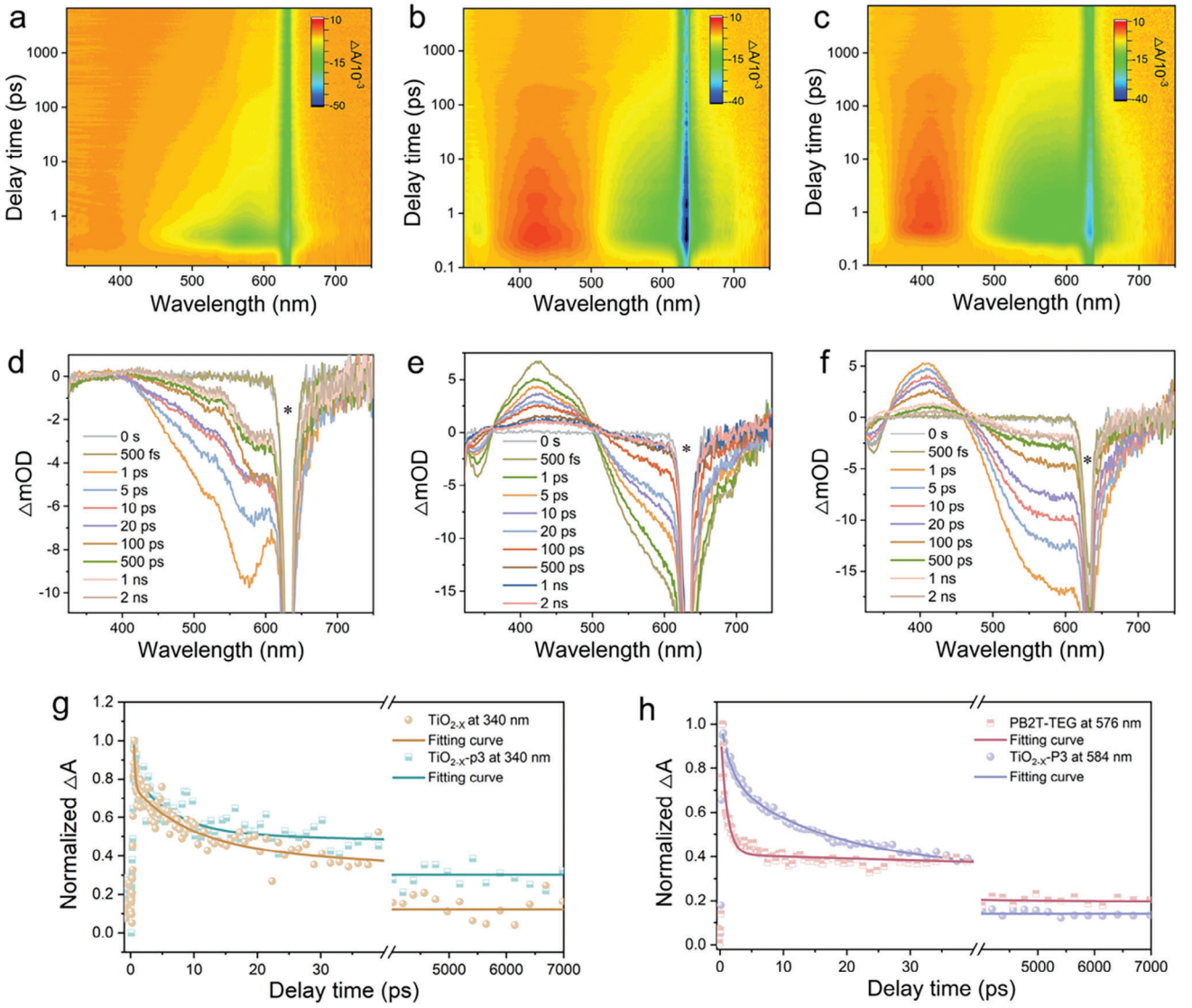

Figure 5. Contour maps of the fs-TA spectra of a) PB2T-TEG, b) TiO_{2-X} and c) TiO_{2-X}-P3 excited at 315 nm, representative spectra at different delay times for d) PB2T-TEG, e) TiO_{2-X} and f) TiO_{2-X}-P3 in the range of 500 fs to 2 ns, where signals marked with a flower belong to the pump light scattering to the detector. Normalized decay kinetic curves of g) TiO_{2-X} and TiO_{2-X}-P3 at 340 nm, h) PB2T-TEG at 576 nm and TiO_{2-X}-P3 at 584 nm.

dark and light irradiation. For the TiO_{2-X} and TiO_{2-X}-P3 systems, no ESR signal of reactive species occurred in the dark reaction. After 5 min of light irradiation, the characteristic peaks of DMPO-$\cdot O_2^-$ were observed (Figure 6c). The signal intensities of $\cdot O_2^-$ radicals captured by TiO_{2-X}-P3 were notably higher than those captured by TiO_{2-X} after 10 min of light irradiation. This indicates that the heterojunction construction endows the photocatalyst with enhanced reduction capabilities. Based on the energy band structure of the photocatalyst, electron–hole separation behavior shown above, and photocatalytic performance, we propose a Type II-scheme model for the transfer of photo-generated electrons in the TiO_{2-X}-P3 heterojunction. Under UV light, the electron transfer takes place from the VB to CB of TiO_{2-X} corresponding to bandgap excitation. After that, the transfer of holes from the VB of TiO_{2-X} to the HOMO of PB2T-TEG occurs, leading to the separation of electrons and holes. Finally, protons are reduced by electrons at the CB of TiO_{2-X} (Figure 6d, left side). On the other hand, under visible light, both PB2T-TEG and TiO_{2-X} are excited, leading to electrons transfer from the LUMO of PB2T-TEG to the CB of TiO_{2-X}, and hole transfer from VB of TiO_{2-X} to HOMO of PB2T-TEG. Thereby, more electrons and holes are generated to facilitate the hydrogen production on the heterojunctions (Figure 6d, right-side). This can be the reason why the photocatalyst achieves high AQY both in the UV and visible regions. Overall, we can conclude that the OEG functionalized conjugated polymer can not only transfer more electrons in the visible region to TiO_{2-X} but also act as a hole trap in ultraviolet light to accelerate the process of photogenerated electrons in TiO_{2-X}, leading to the enhancement of photocatalytic reaction efficiency. The bifunctional polymer-modified inorganic photocatalyst with different optical bands has great potential for enhancing hydrogen production performance.

© 2024 The Author(s). Small published by Wiley-VCH GmbH

16136829, 2024, 43, Downloaded from https://onlinelibrary.wiley.com/doi/10.1002/smll.202402649 by Statens Beredning, Wiley Online Library on [14/11/2024]. See the Terms and Conditions (https://onlinelibrary.wiley.com/terms-and-conditions) on Wiley Online Library for rules of use; OA articles are governed by the applicable Creative Commons License

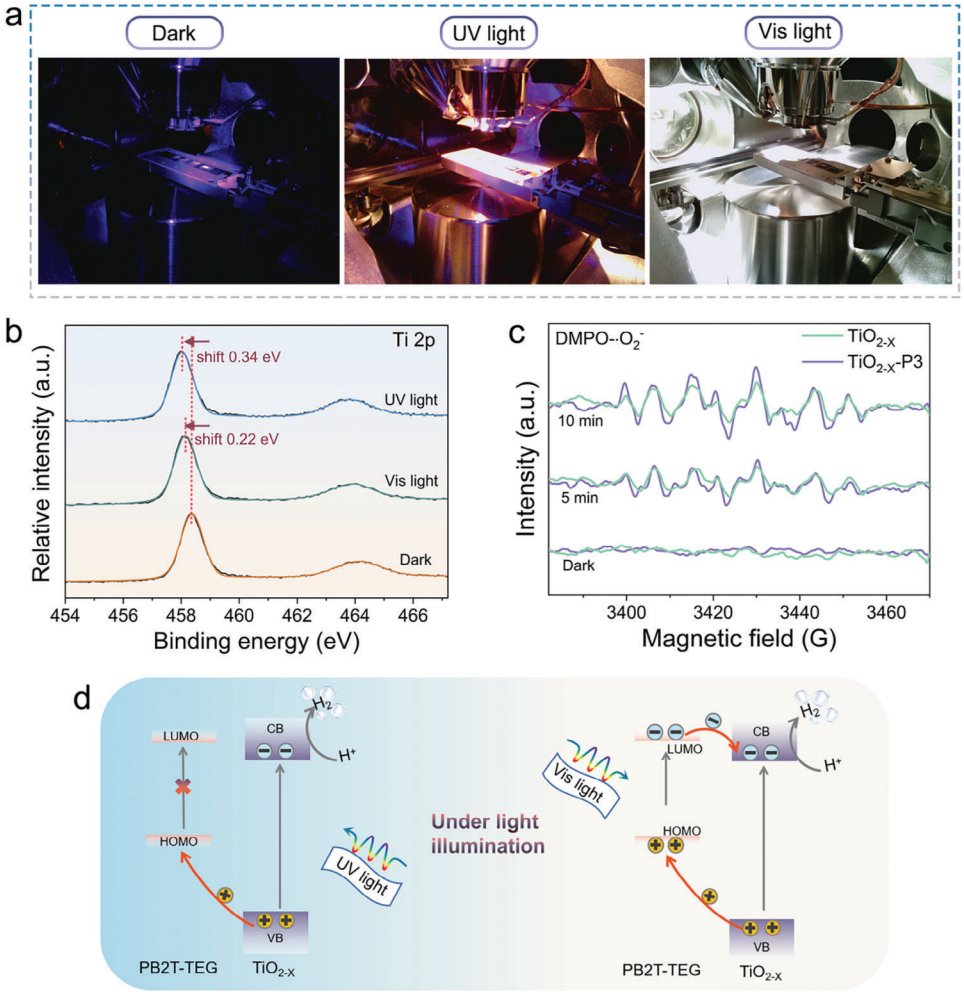

Figure 6. a) Three environments during XPS measurement: Dark, UV light, and Visible light, b) High-resolution in situ XPS for Ti 2p of TiO_{2-X}-P3 in the dark, and under UV and visible irradiation, c) EPR signals of $\cdot O_2^-$ over TiO_{2-X}, and TiO_{2-X}-P3 in the presence of DMPO, d) schematic illustration of the charge transfer under different wavelengths of light irradiation.

3. Conclusion

In summary, we fabricate a composite of TiO_{2-X} coupled to PB2T-TEG forming organic–inorganic heterostructures as efficient photocatalysts with enhanced charge separation and transfer, as compared to the single counterparts, for photocatalytic hydrogen evolution. The TiO_{2-X}-P3 heterojunction (with 3 wt.% of PB2T-TEG) shows a hydrogen evolution rate of 35.7 mmol g^{-1} h^{-1}, which is ≈2.8 and 221 times higher than those of TiO_{2-X} and PB2T-TEG, respectively. Importantly, such high HER is achieved with a loading of only 0.62 wt.% of Pt co-catalyst and an AQY of 53.3% is attained with irradiation at 365 nm. The heterostructured photocatalyst maintains efficient hydrogen production and structural stability during the extended 16-h photocatalytic test. The fs-TA spectroscopy and in situ XPS analysis reveal the charge transfer pathways in heterojunctions at different wavelengths. Therefore, the formation of Type II heterojunction is proposed, facilitating photo-generated efficient charge transfer between PB2T-TEG and TiO_{2-X}. This work opens an avenue to the design and synthesis of organic–inorganic semiconductor heterostructures and provides a deep understanding of the charge-transfer mechanism between the two components.

4. Experimental Section

Preparation of the Polymer PB2T-TEG Photocatalyst: In a dry 50 mL flask, 1,4-dibromo-2,5-bis(2-(2-(2-methoxyethoxy)ethoxy)ethoxy) benzene (362.5 mg, 0.65 mmol), 5,5′-bis(trimethylstannyl)-2,2′-bithiophene (318.2 mg, 0.65 mmol) and $Pd(PPh_3)_4$ (25 mg) were dissolved in anhydrous toluene (8 mL) and DMF (1.5 mL). After purging with nitrogen, the reaction mixture was vigorously stirred at 100 °C for 48 h under a nitrogen atmosphere. After cooling to room temperature, the polymer was precipitated by pouring the solution into hexane, filtered through a Soxhlet thimble, and then subjected to Soxhlet extraction with hexane, methanol, and chloroform. The chloroform fraction was purified by passing it through a short silica gel column and then precipitated from hexane. Finally, the polymer was obtained by filtration through a Teflon filter (0.45 µm) and dried under vacuum at 40 °C overnight (265 mg, 72.3%). Mn = 41 kDa, Đ = 1.5.

Preparation of TiO_2 and TiO_{2-X} MS Photocatalyst: TiO_2 MS was synthesized according to a previous study.[71] An amorphous precursor of TiO_2 was synthesized using a modified sol–gel and solvothermal method.

© 2024 The Author(s). Small published by Wiley-VCH GmbH

16136829, 2024, 43, Downloaded from https://onlinelibrary.wiley.com/doi/10.1002/smll.202402649 by Statens Beredning, Wiley Online Library on [14/11/2024]. See the Terms and Conditions (https://onlinelibrary.wiley.com/terms-and-conditions) on Wiley Online Library for rules of use; OA articles are governed by the applicable Creative Commons License

In this process, 1-hexadecylamine (HDA, 3.84 g) was dispersed in a mixture solution of methanol (750 mL), KCl (6 mL, 0.1 M in H_2O), and Titanium(IV) isopropoxide (13 mL). The mixture was left at room temperature for 15 h without stirring. Subsequently, the obtained product was centrifuged, and washed, and then 0.2 g of the amorphous precursor TiO_2 nanosphere was dispersed in a 40 mL solution containing equal volumes of ethanol and deionized water and sealed in a Teflon-lined stainless steel autoclave. Then, the solution was heated in an autoclave at 160 °C for 15 h, and the TiO_2 MS was rinsed several times with deionized water and ethanol before being dried overnight at 60 °C. The TiO_2 MS was placed in a tubular furnace, calcined with a heating ramp of 10 °C min^{-1} in the 5% H_2/Ar flow to 300 °C, and kept for a duration of 3 h.

Preparation of PB2T-TEG-TiO_{2-X} Photocatalyst: A mass of the PB2T-TEG was dissolved in ethanol to form a homogeneous solution with a concentration of 1 mg mL^{-1} through ultrasonication and stirring. Simultaneously, 10 mg of TiO_{2-X} MS was also dispersed in 10 mL of ethanol by sonication. The PB2T-TEG ethanol solution was then added dropwise to the ethanol dispersion of TiO_{2-X} MS at a specific mass ratio for being stirred and sonicated for 15 min, followed by continuous stirring at 60 °C for half an hour to form a homogeneous mixed solution. The resulting hybrid powder was obtained by vacuum drying at 40 °C to remove the ethanol solvent. The resulting samples could be labeled as TiO_{2-X}-PY (Y = 1, 3, 5, 7 wt.%), where Y refers to the mass ratio of the polymer in hybrid materials. Further, accurate measurement of PB2T-TEG content was performed by ICP-MS as shown in Table S5 (Supporting Information).

Supporting Information

Supporting Information is available from the Wiley Online Library or from the author.

Acknowledgements

The authors acknowledge Myfab Uppsala for providing facilities and experimental support. Myfab was funded by the Swedish Research Council (2019-00207, 2019-04683) as a national research infrastructure. The authors also acknowledge the financial support from the Swedish Energy Agency (grant no. 46641-1, P2021-90067), the Olle Engkvist Foundation (grant no. SOEB-2015/167), the Wenner-Gren Foundations (UPD2021-0123), China Scholarship Council (no. 202206120015) and the Key Laboratory for Ultrafine Materials of the Ministry of Education at East China University of Science and Technology for their financial support. This work is also supported by the National Key Research and Development Program of China under Grant No. 2019YFA0705201. Furthermore, the authors would like to thank Yaqi Li, Tianyuan Chen, Ming Liu, Qianhui Liu, Zeng Zhi, and Taha Ahmed for their very kind help with equipment training and material characterization.

Conflict of Interest

The authors declare no conflict of interest.

Data Availability Statement

The data that support the findings of this study are available from the corresponding author upon reasonable request.

Keywords

charge carrier separation, conjugated polymers, organic–inorganic heterojunctions, photocatalytic hydrogen evolution reactions, TiO_{2-X}

Received: April 3, 2024
Revised: June 3, 2024
Published online: July 1, 2024

[1] J. Su, L. Vayssieres, *ACS Energy Lett.* **2016**, *1*, 121.
[2] C. Guo, D. Li, L. Wang, B. Du, Z. X. Liu, Z. Shen, P. Wang, X. Zhang, J. Cai, S. Cheng, C. Yu, H. Wang, D. Liu, C. Z. Li, T. Wang, *Adv. Energy Mater.* **2021**, *11*, 2102000.
[3] Y. Bai, K. Hippalgaonkar, R. S. Sprick, *J. Mater. Chem. A* **2021**, *9*, 16222.
[4] A. Listorti, J. Durrant, J. Barber, *Nat. Mater.* **2009**, *8*, 929.
[5] J. Rongé, T. Bosserez, D. Martel, C. Nervi, L. Boarino, F. Taulelle, G. Decher, S. Bordig, J. A. Martens, *Chem. Soc. Rev.* **2014**, *43*, 7963.
[6] N. S. Lewis, *Science* **2016**, *351*, 6271.
[7] J. H. Kim, D. Hansora, P. Sharma, J. W. Jang, J. S. Lee, *Chem. Soc. Rev.* **2019**, *48*, 1908.
[8] T. Hisatomi, K. Domen, *Nat. Catal.* **2019**, *2*, 387.
[9] M. E. El-Khouly, E. El-Mohsnawy, S. Fukuzumi, *J. Photochem. Photobiol. C* **2017**, *31*, 36.
[10] Y. M. Zhu, L. Zhang, B. Zhao, H. J. Chen, X. Liu, R. Zhao, X. W. Wang, J. Liu, Y. Chen, M. Liu, *Adv. Funct. Mater.* **2019**, *29*, 1901783.
[11] R. Nazanin, P. Randolph, G. Evan, *Prog. Solid. State Chem.* **2019**, *55*, 1.
[12] T. Iwaki, *J Chem. Soc.* **1983**, *79*, 137.
[13] L. Zhang, R. H. Li, X. X. Li, Y. Q. Lan, *Proc. Natl. Acad. Sci. USA* **2022**, *119*, 2210550119.
[14] Q. Wang, T. Hisatomi, Q. Jia, H. Tokudome, M. Zhong, C. Wang, Z. Pan, T. Takata, M. Nakabayash, N. Shibata, Y. Li, I. Sharp, A. Kudo, T. Yamada, K. Domen, *Nat. Mater.* **2016**, *15*, 611.
[15] M. Liras, M. Barawi, V. A. de la Peña O'Shea, *Chem. Soc. Rev.* **2019**, *48*, 5454.
[16] L. Collado, T. Naranjo, M. Gomez-Mendoza, C. G. López-Calixto, F. Oropeza, M. Liras, J. Marugán, V. de la Peña O'Shea, *Adv. Funct. Mater.* **2021**, *31*, 2105384.
[17] T. Zhang, G. Xing, W. Chen, L. Chen, *Mater. Chem. Front.* **2020**, *4*, 332.
[18] R. R. Haikal, A. B. Soliman, M. Amin, S. G. Karakalos, Y. S. Hassan, A. M. Elmansi, I. H. Hafez, M. R. Berber, A. Hassanien, M. H. Alkordi, *Appl. Catal. B* **2017**, *207*, 347.
[19] C. X. Zhao, Z. P. Chen, R. Shi, X. F. Yang, T. R. Zhang, *Adv. Mater.* **2020**, *32*, 1907296.
[20] C. Yang, B. C. Ma, L. Zhang, S. Lin, S. Ghasimi, K. Landfester, K. A. Zhang, X. Wang, *Angew. Chem., Int. Ed.* **2016**, *55*, 9202.
[21] L. Jiang, X. Yuan, Y. Pan, J. Liang, G. Zeng, Z. Wu, H. Wang, *Appl. Catal. B* **2017**, *217*, 388.
[22] R. S. Sprick, L. Wilbraham, Y. Bai, P. Guiglion, A. Monti, R. Clowes, A. I. Cooper, M. A. Zwijnenburg, *Chem. Mater.* **2018**, *30*, 5733.
[23] X. H. Zhang, X. P. Wang, J. Xiao, S. Y. Wang, D. K. Huang, X. Ding, Y. G. Xiang, H. Chen, *J. Catal.* **2017**, *350*, 64.
[24] R. S. Sprick, B. Bonillo, R. Clowes, P. Guiglion, N. J. Brownbill, B. J. Slater, F. Blanc, M. A. Zwijnenburg, D. J. Adams, A. I. Cooper, *Angew. Chem., Int. Ed.* **2018**, *57*, 2520.
[25] M. Barawi, L. Collado, M. Gomez-Mendoza, F. E. Oropeza, M. Liras, V. A. de la Peña O'She, *Adv. Energy Mater.* **2021**, *18*, 2101530.
[26] V. W. H. Lau, I. Moudrakovski, T. Botari, S. Weinberger, M. B. Mesch, V. Duppel, J. Senker, V. Blum, B. V. Lotsch, *Nat. Commun.* **2016**, *7*, 12165.
[27] K. Li, L. Wang, Z. X. Chen, X. F. Yang, Y. X. Yu, W. D. Zhang, Y. Wang, Y. M. Shi, K. P. Loh, Q. H. Xu, *Adv. Funct. Mater.* **2020**, *30*, 2005106.
[28] B. Wang, W. Song, D. Li, X. Long, Y. Xia, *J. Mater. Chem. A* **2021**, *9*, 3322.
[29] M. E. Cinar, T. Ozturk, *Chem. Rev.* **2015**, *115*, 3036.
[30] B. Chen, H. Zhang, W. Luo, H. Nie, R. Hu, A. Qin, Z. Zhao, B. Z. Tang, *J. Mater. Chem. C* **2017**, *5*, 960.
[31] C. Duan, K. Zhang, C. Zhong, F. Huang, Y. Cao, *Chem. Soc. Rev.* **2013**, *42*, 9071.
[32] Z. C. Hu, Z. F. Wang, X. Zhang, H. R. Tang, X. C. Liu, F. Huang, Y. Cao, *iScience* **2019**, *13*, 33.

© 2024 The Author(s). Small published by Wiley-VCH GmbH

16136829, 2024, 43, Downloaded from https://onlinelibrary.wiley.com/doi/10.1002/smll.202402649 by Statens Beredning, Wiley Online Library on [14/11/2024]. See the Terms and Conditions (https://onlinelibrary.wiley.com/terms-and-conditions) on Wiley Online Library for rules of use; OA articles are governed by the applicable Creative Commons License

[33] J. Kosco, S. Gonzalez-Carrero, C. T. Howells, W. Zhang, M. Moser, R. Sheelamanthula, L. Zhao, B. Willner, T. C. Hidalgo, H. Faber, B. Purushothaman, M. Sachs, H. Cha, R. Sougrat, T. D. Anthopoulos, S. Inal, J. R. Durrant, I. McCulloch, *Adv. Mater.* **2022**, *34*, 2105007.
[34] C. A. Traina, R. C. Bakus, G. C. Bazan, *J. Am. Chem. Soc.* **2011**, *133*, 12600.
[35] P. J. Tseng, C. L. Chang, Y. H. Chan, L. Y. Ting, P. Y. Chen, C. H. Liao, M.-L. Tsai, H. H. Chou, *ACS Catal.* **2018**, *8*, 7766.
[36] M. D. Hernandez-Alonso, F. Fresno, S. Suarez, J. M. Coronado, *Energy Environ. Sci.* **2009**, *2*, 1231.
[37] Z. P. Xing, J. Q. Zhang, J. Y. Cui, J. W. Yin, T. Y. Zhao, J. Y. Kuang, Z. Y. Xiu, N. Wan, W. Zhou, *Appl. Catal. B Environ.* **2018**, *225*, 452.
[38] Y. Bai, I. Mora-Seró, F. De Angelis, J. Bisquert, P. Wang, *Chem. Rev.* **2014**, *114*, 10095.
[39] S. Oh, J. Kim, H. Hwang, D. Kim, J. Kim, G. Park, J. Kim, Y. Lee, H. Lee, *J. Mater. Chem. A* **2021**, *9*, 4822.
[40] B. J. Sun, J. Q. Bu, Y. C. Du, X. Y. Chen, Z. Z. Li, W. Zhou, *ACS Appl. Mater. Interfaces* **2021**, *13*, 37545.
[41] C. Wang, T. N. Zhang, L. F. Yin, C. S. Ni, J. P. Ni, L. A. Hou, *Chemosphere* **2022**, *86*, 131804.
[42] J. M. Cai, M. Q. Wu, Y. T. Wang, H. Zhang, M. Meng, Y. Tian, X. G. Li, J. Zhang, L. R. Zheng, J. L. Gong, *Chem* **2017**, *2*, 877.
[43] T. Lin, C. Yang, Z. Wang, H. Yin, X. Lu, F. Huang, J. Lin, X. Xie, M. Jiang, *Energy Environ. Sci.* **2014**, *7*, 967.
[44] C. G. Bischak, L. Q. Flagg, K. Yan, T. Rehman, D. W. Davies, R. J. Quezada, J. W. Onorato, C. K. Luscombe, Y. Diao, C. Z. Li, D. S. Ginger, *J. Am. Chem. Soc.* **2020**, *142*, 7434.
[45] Y. Q. Xing, Z. R. Tan, J. Z. Cheng, Z. Q. Shen, Y. J. Zhang, L. Chen, S. Y. Liu, *Sustain. Energy Fuels* **2021**, *5*, 5166.
[46] R. R. Jiang, G. H. Lu, T. J. Dang, M. Wang, J. C. Liu, Z. H. Yan, H. J. Xie, *Chem. Eng. J* **2023**, *454*, 140018.
[47] L. Zhang, T. Chiang Albert Ng, X. M. Liu, Q. L. Gu, Y. J. Pang, Z. X. Zhang, Z. Y. Lyu, Z. M. He, H. Y. Ng, J. Wang, *Appl. Catal. B-Environ.* **2020**, *264*, 118528.
[48] H. W. Huang, K. Liu, Y. L. Zhang, K. Chen, Y. H. Zhang, N. Tian, *RSC Adv.* **2014**, *4*, 4938.
[49] H. Q. Tan, Z. Zhao, M. Niu, C. Y. Mao, D. P. Cao, D. J. Cheng, P. Y. Feng, Z. C. Sun, *Nanoscale* **2014**, *6*, 10216.
[50] A. J. Henegar, T. Gougousi, *ECS J. Sol. State Sci. Technol.* **2015**, *4*, P298.
[51] Z. L. Sun, V. F. Pichugin, K. E. Evdokimov, M. E. Konishchev, M. S. Syrtanov, V. N. Kudiiarov, K.e Li, S. I. Tverdokhlebov, *Appl. Surf. Sci.* **2020**, *500*, 144048.
[52] Z. Lan, W. Ren, X. Chen, Y. F. Zhang, X. C. Wang, *Appl. Catal. B* **2019**, *245*, 596.
[53] Y. P. Zhang, W. Han, Y. Yang, H. Y. Zhang, Y. Wang, L. Wang, X. J. Sun, F. M. Zhang, *Chem. Eng. J.* **2022**, *446*, 137213.
[54] M. Zhang, M. Lu, Z. L. Lang, J. Liu, M. Liu, J. N. Chang, L. Y. Li, L. J. Shang, M. Wang, S. L. Li, Y. Q. Lan, *Angew. Chem., Int. Ed.* **2020**, *59*, 6500.
[55] A. Naldoni, M. Altomare, G. Zoppellaro, N. Liu, S. Kment, Ŕ. Zboril, P. Schmuki, *ACS Catal.* **2019**, *9*, 345.
[56] H. H. Gao, R. Cao, X. T. Xu, S. W. Zhang, Y. S. Huang, H. C. Yang, X. L. Deng, J. X. Li, *Appl. Catal. B-Environ.* **2019**, *245*, 399.
[57] C. M. Li, H. H. Wu, D. Q. Zhu, T. X. Zhou, M. Yan, G. Chen, J. X. Sun, G. Dai, F. Ge, H. J. Dong, *Appl. Catal. B-Environ.* **2021**, *297*, 120433.
[58] D. Carta, G. Mountjoy, A. Regoutz, A. Khiat, A. Serb, T. Prodromakis, *J. Phys. Chem. C* **2015**, *119*, 4362.
[59] L. Liu, X. Chen, *Chem. Rev.* **2014**, *114*, 9890.
[60] N. Tian, Y. H. Zhang, X. W. Li, K. Xiao, X. Du, F. Dong, G. I. N. Waterhouse, T. R. Zhang, H. W. Huang, *Nano Energy* **2017**, *38*, 72.
[61] W. B. Chen, L. Wang, D. Mo, F. He, Z. L. Wen, X. J. Wu, H. X. Xu, L. Chen, *Angew. Chem., Int. Ed.* **2020**, *59*, 16902.
[62] H. L. Cui, W. Zhao, C. Y. Yang, H. Yin, T. Q. Lin, Y. F. Shan, Y. Xie, H. Gu, F. Q. Huang, *J. Mater. Chem. A* **2014**, *2*, 8612.
[63] Y. C. Wang, W. B. Hao, H. Liu, R. Z. Chen, Q. Y. Pan, Z. B. Li, Y. J. Zhao, *Nat. Commun.* **2022**, *13*, 100.
[64] Y. Xia, B. C. Zhu, L. Y. Li, W. K. Ho, J. S. Wu, H. M. Chen, J. G. Yu, *Small* **2023**, *19*, 2301928.
[65] Y. Z. Zhang , Y. K. Li , X. Xin, Y. J. Wang, P. Guo , R. L. Wang, B. L. Wang, W. J. Huang , A. J. Sobrido , X. H. Li, *Nat. Energy* **2023**, *8*, 504.
[66] S. E. Braslavsky, A. M. Braun, A. E. Cassano, A. V. Emeline, M. I. Litter, L. Palmisano, V. N. Parmon, N. Serpone, *Pure Appl. Chem.* **2011**, *83*, 931.
[67] A. Piccioni, D. Catone, A. Paladini, P. O. Keeffe, A. Boschi, A. Kovtun, M. Katsikini, F. Boscherini, L. Pasquini, *J. Phys. Chem. C* **2020**, *124*, 26572.
[68] Y. Y. Jin, H. Y. Xiang, H. L. Jiang, X. C. Liu, J. Sun, Y. X. Feng, Y. Jiang, A. Pan, S. Liu, *Small* **2024**, *20*, 2304010.
[69] A. V. Gonzalez, C. G. L. Calixto, M. Barawi, M. G. Mendoza, V. A. de la Pena O'Shea, M. Liras, B. Gomez-Lor, M. Iglesias, *ACS Appl. Energy Mater.* **2020**, *3*, 4411.
[70] C. Cheng, J. J. Zhang, B. C. Zhu, G. J. Liang, L. Y. Zhang, J. G. Yu, *Angew. Chem., Int. Ed.* **2023**, *62*, 202218688.
[71] B. K. Zhang, D. B. Wang, S. J. Jiao, Z. K. Xu, Y. X. Liu, C. C. Zhao, J. W. Pan, D. H. Liu, G. Liu, B. J. Jiang, Y. F. Li, L. C. Zhao, J. Z. Wang, *Chem. Eng. J.* **2022**, *446*, 137138.

© 2024 The Author(s). Small published by Wiley-VCH GmbH

16136829, 2024, 43, Downloaded from https://onlinelibrary.wiley.com/doi/10.1002/smll.202402649 by Statens Beredning, Wiley Online Library on [14/11/2024]. See the Terms and Conditions (https://onlinelibrary.wiley.com/terms-and-conditions) on Wiley Online Library for rules of use; OA articles are governed by the applicable Creative Commons License